

Wave function description of conductance mapping for quantum Hall electron interferometer

K. Kolasinski and B. Szafran
 AGH University of Science and Technology,
 Faculty of Physics and Applied Computer Science,
 al. Mickiewicza 30, 30-059 Kraków, Poland
 (Dated: February 29, 2024)

Scanning gate microscopy of quantum point contacts (QPC) in the integer quantum Hall regime is considered in terms of the scattering wave functions with a finite-difference implementation of the quantum transmitting boundary approach. Conductance (G) maps for a clean QPC as well as for a system including an antidot within the constriction are evaluated. The step-like locally flat G maps for clean QPCs turn into circular resonances that are reentrant in external magnetic field when the antidot is introduced to the constriction. The current circulation around the antidot and the spacing of the resonances at the magnetic field scale react to the probe approaching the QPC. The calculated G maps with a rigid but soft antidot potential reproduce the features detected recently in the electron interferometer [F. Martins et al. Nature Sci. Rep. **3**, 1416 (2013)].

I. INTRODUCTION

Transport properties of devices based on two-dimensional electron gas in the integer quantum Hall regime are determined by uncompensated currents that are carried by the edges of the sample.¹ The edge states have a very large coherence length¹ and they can be used for construction of electron interferometers.^{2,3} Each of the edges carry the current in a single direction only and the backscattering⁴ at high magnetic field requires electron transfer from one edge to the other across the bulk of the sample. The interedge tunneling paths can be opened at constrictions (quantum point contacts QPCs) which are intentionally introduced to the channel. A pair of QPCs with an internal cavity⁵ form a setup which is referred to as quantum Hall,^{6–8} electronic Fabry-Pérot^{9–11} or Aharonov-Bohm (AB) interferometer.^{12–14} The latter reference is due to the periodicity of conductance (G) in external magnetic field for the currents following the edges of the cavity. A similar interference mechanism and periodic G behavior is found for an antidot introduced between the edges of the sample^{7,16–22} with electron currents encircling the antidot.

At low magnetic field the electron currents passing through a quantum point contact can be mapped^{23–27} by the scanning gate microscopy²⁸ which measures conductance as functions of the position of the atomic force microscope tip moving above the sample. The charged tip is capacitively coupled to the electron gas and modifies the local potential landscape. In particular a clear semi-classical magnetic focusing²⁹ of electron currents at a field of a fraction of Tesla was observed. The magnetic fields of the order of mT lift the interference pattern of G maps of QPC that appear according to the weak localization mechanism.³⁰ At higher magnetic fields, within the quantum Hall regime the currents evade a direct mapping bypassing any potential perturbations introduced by the tip. The conductance in the quantum Hall regime can still be affected by the tip when it enhances the inter-edge

tunnel coupling,^{31,32} depopulate the edge states within QPC,³³ or allow for selective control of individual edge channels.³⁰

Scanning gate microscopy^{7,8} was used for detection of the charging effects^{10,34,35} of the Coulomb island in the interferometer including an intentionally introduced antidot. Recently,³⁶ a spontaneous formation of an interferometer with a quantum Hall island (QHI) located inside a quantum point contact was demonstrated by the scanning gate microscopy. Simulations of the coherent transport in similar conditions are the purpose of the present work. To the best of our knowledge we provide the first wave function description of the scanning gate microscopy mapping of the coherent flow across the electron interferometer. The QHI is modeled as an antidot with a fixed potential. We discuss formation of current loops around the QHI which is reentrant in function of the magnetic field. We describe perturbation to the current flow pattern introduced by the tip and the consequences of bridging the edge currents by the tip for conductance. The present numerical simulations reproduce the step-like character of experimental^{30,33,37} integer quantum Hall G maps for clean QPCs with flat minima near the QPCs and no distinct features for the tip outside of the QPC. Calculations for the electron interferometer reproduce the characteristics of experimental SGM maps,³⁶ including the circular form of oscillations in the G map, the shifts of resonant lines to lower values of B by the repulsive tip as well as the reduction of the G periodicity for the tip approaching the QHI. We demonstrate that the latter occurs only when the potential of the QHI potential has a soft profile.

Below we discuss the periodicity of the conductance oscillations. The early experiments^{5,17} on electron interferometers in the integer quantum Hall regime detected the Aharonov-Bohm periodicity with period $\Delta B = \Phi_0/S$, where $\Phi_0 = e/h$ is the flux quantum and S is the area encircled by the currents. Subsequent studies^{14,15} reported fractional periodicity with $\Delta B = \Phi_0/(f_c S)$, where f_c is the number of edge modes fully transmitted across the

sample. The fractional periodicity of AB conductance oscillations in electron interferometers are explained as due to the electron-electron interaction.⁶ The interaction effects leading to fractional periodicity are outside the range of mean field description^{12,16} which reproduces the $\Delta B = \Phi_0/S$ period. The present calculation neglects the electron-electron interaction and in consequence the integer periodicity is found for any f_c . We focus on the qualitative changes of the AB period that are due to the presence of the tip which are independent of f_c .

II. MODEL

We consider a wide channel with a narrowing that is presented in Fig. 1. The channel has a width of 600 nm that is reduced to 200 nm within the QPC. We assume that the narrowing has a Gaussian shape (aspect ratio is preserved in Fig. 1). The length of the computational box is 2000 nm.

The Fermi level electron within the system is described by a two-dimensional effective-mass Schrödinger equation

$$\left[\frac{1}{2m_{\text{eff}}} (-i\hbar\nabla + e\mathbf{A})^2 + V(x, y) \right] \Psi(x, y) = E_F \Psi(x, y), \quad (1)$$

with the total potential $V(x, y) = V_c(x, y) + V_{\text{tip}}(x, y) + V_{\text{QHI}}(x, y)$, where V_c is the confinement potential (we assume an infinite potential outside the channel and zero in the inside), V_{tip} is the tip potential and V_{QHI} is the potential that models the quantum Hall island within the QPC. We consider a GaAs system with the effective electron band mass $m_{\text{eff}} = 0.067m_0$. The spin Zeeman effect for B of the order of 1 T is still weak in GaAs and is neglected in the calculations.

The original potential of the tip as seen by the two-dimensional electron gas is of the Coulomb form. This potential is screened by deformation of the gas.³⁸ In consequence the potential as seen by the Fermi level electrons is short-range. Our previous Schrödinger-Poisson calculations^{38–40} indicated that the effective tip potential is close to Lorentzian with the width of the order of the distance between the tip and the electron gas. Accordingly, in this paper we use the Lorentz model of the potential

$$V_{\text{tip}}(x, y) = \frac{U_{\text{tip}}}{1 + \left((x - x_{\text{tip}})^2 + (y - y_{\text{tip}})^2 \right) / d_{\text{tip}}^2}, \quad (2)$$

for the tip localized above point $(x_{\text{tip}}, y_{\text{tip}})$. We use $d_{\text{tip}} = 60$ nm for the width of the tip potential. The potential of the quantum Hall island is also taken in the Lorentz form

$$V_{\text{QHI}}(x, y) = \frac{U_{\text{QHI}}}{1 + \left((x - x_{\text{QHI}})^2 + (y - y_{\text{QHI}})^2 \right) / d_{\text{QHI}}^2}, \quad (3)$$

we assume that the QHI is located in the center of the constriction (see Fig. 1) with $x_{\text{QHI}} = 1000$ nm and $y_{\text{QHI}} = 0$.

We choose the Lorentz gauge $\mathbf{A} = (-By, 0, 0)$ for the uniform magnetic field applied perpendicular to the plane of confinement. The brown areas at the ends of the computational box in Fig. 1 denote the asymptotic regions where the boundary conditions are introduced. The calculation method applied here is a variant of the one used previously in Ref. 38. We use the gauge-invariant kinetic-energy discretization,⁴¹ which leads to the following finite difference equation

$$\begin{aligned} & \Psi_{u,v} (4t_0 + V_{u,v} - E_F) + \Psi_{u+1,v} (-t_0 C_x^*) \\ & + \Psi_{u-1,v} (-t_0 C_x) + \Psi_{u,v-1} (-t_0) + \Psi_{u,v+1} (-t_0) = 0, \end{aligned} \quad (4)$$

where $C_x = e^{-i\frac{e}{\hbar}\Delta x A_x}$, and $t_0 = 1/(2m_{\text{eff}}\Delta x^2)$. For the considered magnetic fields and Fermi wave vectors, convergent results are obtained for $\Delta x = \Delta y = 2$ nm.

Equation (4) defines a set of linear equations for the wave function in the interior of the computational box. The boundary conditions for the scattering problem are set in the following way. In the leads far away from the QPC and the tip potential, the confinement potential is independent of x , i.e. $V(x, y) \rightarrow V(y)$, thus we can write the asymptotic Hamiltonian eigenfunctions as superpositions of plane waves multiplied by transverse modes χ_k . Far away from the scattering region – beyond the range of the evanescent modes – the wave function takes the form⁴²

$$\Psi(x, y) = \sum_{k=1}^M a_k e^{ikx} \chi_k(y) + b_k e^{-ikx} \chi_{-k}(y), \quad (5)$$

where M is the number of subbands at the Fermi level, k is the real wave vector, $\chi_k(y)$ [$\chi_{-k}(y)$] represents the k -th incoming (backscattered) transverse mode. The transverse modes are found by solving the eigenproblem for the homogeneous lead.³⁸ The coefficients a_k and b_k correspond to the incoming and the outgoing amplitudes, respectively. At the output lead we can write the solution in the form of superposition of outgoing modes

$$\Psi(x, y) = \sum_{k=1}^M d_k e^{ikx} \chi_k(y), \quad (6)$$

where d_k is the amplitude of outgoing mode χ_k . The method applied in Refs. 38–40 used an iterative scheme for evaluation of the scattering amplitudes. Here we get rid of the iteration employing the quantum transmitting boundary (QTB) which was originally developed^{43,44} for the finite element method. Here we adapt QTB for the finite difference method. The details of the present calculation are given in the Appendix. A similar procedure has been applied recently in Ref. 45 for the current flow through ballistic nanodevices but in the absence of magnetic field.

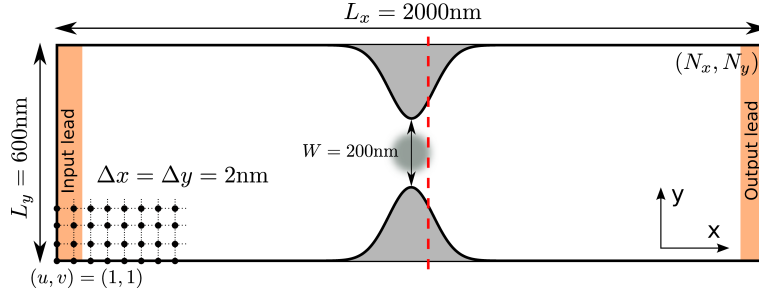


Figure 1: (color online) Sketch of the QPC system considered in this paper. The dots in the left corner show the finite difference mesh used in numerical calculations. The vertical dashed red line shows the path of the conductance scan discussed in the text. The gray area in the center of QPC indicates a local potential maximum introduced to model the quantum Hall island.

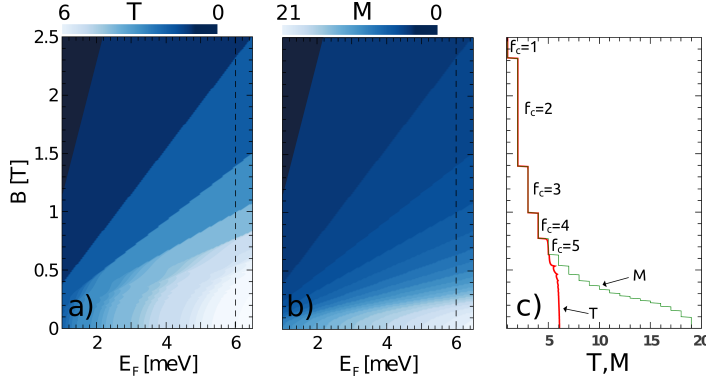


Figure 2: (a) Transfer probability through the QPC summed over the incident subbands [Eq. (7)] and (b) the number of transport modes M in the leads as functions of Fermi energy E_F and the perpendicular magnetic field B . The dashed lines on both plots show the energy value $E_F = 6$ meV which is considered further in this paper. (c) Cross section of (a) and (b) for $E_F = 6$ meV.

After solution of the quantum scattering problem we evaluate the conductance by the Landauer-Büttiker formula

$$G = \frac{e^2}{h} T = \frac{e^2}{h} \sum_i^M T_i, \quad (7)$$

where T_i is the transmission probability of the i 'th mode incident from the input lead. The transmission T_i for each incoming mode is calculated in the following way. For a given incoming mode i we set the incoming amplitudes to $a_k = \delta_{ik}$, where $k = (1, \dots, M)$. We solve the Schrödinger equation (4) with transmitting boundary conditions (see Appendix). Then, we calculate incoming b_k and outgoing d_k amplitudes (Appendix). Finally, the transmission probability is calculated from the probability current fluxes

$$T_i = \sum_{k=1}^M \frac{|d_k|^2 \sum_{v=1}^{N_y} |\chi_k(v)|^2 \sin\left(\frac{e}{\hbar} \Delta x^2 v B + k \Delta x\right)}{\sum_{v=1}^{N_y} |\chi_i(v)|^2 \sin\left(\frac{e}{\hbar} \Delta x^2 v B + k_i \Delta x\right)}, \quad (8)$$

where k_i stands for the wave vector of the i 'th incoming mode and the expression $\sum_{v=1}^{N_y} |\chi_k(v)|^2 \sin\left(\frac{e}{\hbar} \Delta x^2 v B + k \Delta x\right)$ corresponds to the probability flux of a given mode (with $k > 0$).

III. RESULTS

A. G maps for a clean QPC

Figure 2(a) demonstrates the transfer probability summed over the subbands [Eq. (7)] as a function of the magnetic field B and the Fermi energy E_F . The $T(B, E_F)$ function exhibits a step-like behavior with reduction of the number of the transport modes with increasing B or lowering E_F . The results of Fig. 2(a) are obtained from solution to the scattering problem involving M subbands in the leads – see Fig. 2(b) which appear at the Fermi level for a given B . For the further discussion we choose Fermi energy equal to 6 meV.

The G map obtained for $B = 0.9$ T for the clean QPC is presented in Fig. 3(a). The conductance is reduced from $f_c = 4$ to $f_c = 3$ when the tip approaches the area of the QPC. Note, that when the tip is outside the QPC the G map ignores its presence. The flat minimum of G within the QPC and the insensitiveness of the map to the position of the tip when its outside the constriction is a characteristic feature of experimental maps obtained in SGM imaging of the edge states in QPCs – see Ref. 33 of Ref. 30 [Fig. 4]. Note that in contrast to the integer quantum Hall regime, for $B = 0$ the G maps

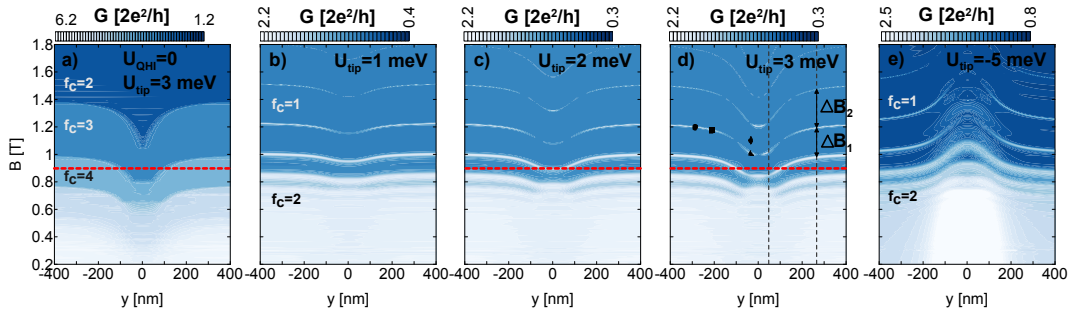


Figure 3: Conductance maps obtained for $B = 0.9$ T and different values of U_{tip} (a) without QHI, and (b-d) with QHI within QPC.

collected from the outside of the QPC contain fine details with resolved branches^{24,30} as well as interference fringes²⁶ involving backscattering by the tip. For high B the backscattering is only allowed for the tip forming bridges between the conducting sample edges, hence the flat region of the G map outside the QPC.

Figure 4(a) shows the conductance for the tip scanning across the channel close to QPC along the red dashed line in Fig. 1 with varying magnetic field. In the absence of the tip the $G(B)$ dependence has a step-like character [see Fig. 2(a)] in consistence with the experimental results of Ref. 33 [Fig. 2(f)] and the ones of Ref. 30 [Fig. 4] and Ref. 37 [Fig. 1(a)]. When the repulsive tip approaches the axis of the QPC ($y \simeq 0$) it enhances the backscattering and induces shifts of G steps to lower values of B . The experimental result for the equivalent measurement with QHI inside the constriction [Fig. 2(a) of Ref. 36] exhibits oscillations of G instead of steps that appear in the result of Fig. 2(a).

B. G maps for the interferometer

In search for the oscillatory behavior of conductance in function of the tip position we have introduced a local potential maximum to the center of the QPC in order to simulate the quantum Hall island³⁶ with radius $d_{\text{QHI}} = 40$ nm [see Eq. (3)]. The results for the transfer probability as a function of the magnetic field and the height of the QHI potential perturbation are given in Fig. 5. For low B an increase of U_{QHI} monotonically reduces the conductance. However, at higher B oscillations of conductance appear. The period of these oscillations decreases with U_{QHI} (see the red arrows), which suggests that the resonances correspond to currents circulating around the QHI with area increasing with the value of the local potential maximum. The currents in the selected locations of the (B, U_{QHI}) diagram were presented in Fig. 5(b-g). In all the plots we find that the current approaches the QPC along the upper edge and is partially backscattered to the lower one. The transmitted current stays close to the upper edge. The area of the QHI is surrounded by an anticlockwise cur-

rent with the electron density pushed to the left of the current direction in consistence with the classical Lorentz force orientation.⁴⁶ We find that the loops of current are fully developed for both G resonances [Fig. 5(b-d)] and antiresonances [5(g,f)]. Outside the resonances and antiresonances the current vortex is weak [Fig. 5(e)]. We conclude that the presence of a potential defect inside the QPC leads to formation of closed current loops which is reentrant in function of B for values of the magnetic field which are more or less periodically spaced. The current loops are coupled to the edge currents, hence the periodic features of conductance. For the further discussion we fix $U_{\text{QHI}} = 11$ meV for which $f_c \geq 1$ for B up to 2.2 T.

The G maps obtained for $B = 0.9$ T for the QHI present inside the QPC are displayed in Fig. 3(b-d). Instead of a central flat minimum of conductance found for the clean QPC [Fig. 3(a)] a resonant ring localized around the QHI defect is detected in agreement with the experimental results.³⁶ The radius of the ring increases with U_{tip} .

Figures 4(b-d) show scans of conductance along the line at a side of the QPC [see Fig. 1] for the increasing value of the tip potential. Already for the tip outside the channel ($y=400$ nm), the conductance exhibits peaks which reappear nearly periodically as functions of B [Fig. 5]. The repulsive tip changes the position of the resonances shifting them to lower magnetic field [Fig. 4(b-d)] in accordance with the experiment.³⁶ An opposite shift is found for the attractive tip [Fig. 4(e)].

In Fig. 6 we plotted the current distribution for three points following the resonance of Fig. 4(d) that are marked by ($\circ, \square, \triangle$) and one point (\diamond) outside the resonance [Fig. 4(e)]. The resonances are related to the interference with current circulating around the QHI. The repulsive tip potential increases the area encircled by the current when placed near the QHI [cf. Fig. 7(a) and Fig. 7(c)]. In consequence, we find that the period of the oscillations is reduced [see Fig. 7] when the tip is near QPC. Note, that for fixed B the tip even when far from the center of the QPC destroys the resonant current loop while moving along the straight line (note the radial form of G map of Fig. 3). In the discussed plots of Fig.

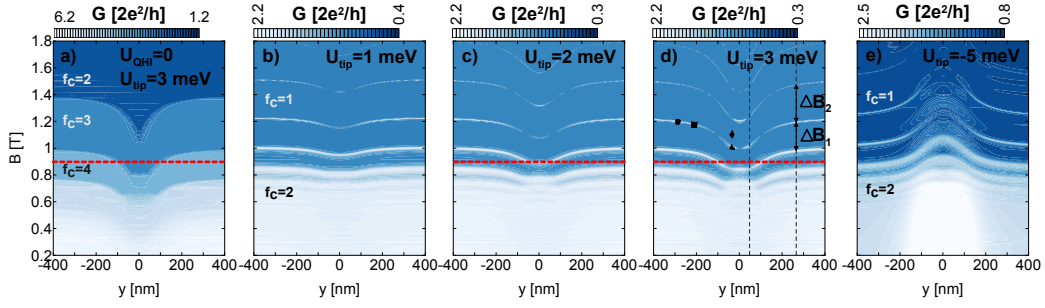


Figure 4: Conductance for $E_F = 6$ meV as a function of the y position of the tip and the magnetic field. The scans were performed along $x_{\text{tip}} = 1100$ nm line (see Fig. 1) with $d_{\text{tip}} = 60$ nm for different values of the tip potential U_{tip} (Eq. 2). (a) Scan of the QPC obtained with $U_{\text{tip}} = 3$ meV and $U_{\text{QHI}} = 0$ (in the absence of QHI). (b-e) Scans obtained for QHI present with: $U_{\text{QHI}} = 11$ meV and $d_{\text{QHI}} = 40$ nm (Eq. 3) for $U_{\text{tip}} = 1, 2, 3$ and -5 meV.

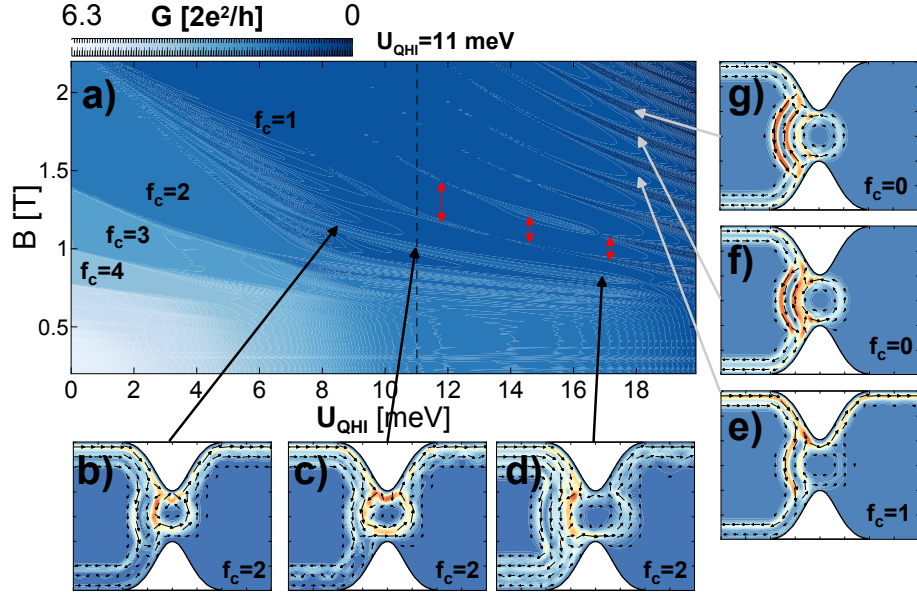


Figure 5: (a) Transfer probability as a function of the amplitude U_{QHI} and magnetic field for $d_{\text{QHI}} = 40$ nm and the center of the potential maximum located at the center of QPC [see Fig.1]. The number of fully transparent subbands f_c is given. The vertical dashed line present the value of U_{QHI} which chose for further calculations. (b-g) Probability density current distribution (color scale shows the absolute value, and vectors the orientation of the current) for various points along resonances with locations indicated by arrows.

5(b-f) the values of B had to be changed to follow the resonance. Moreover, for the attractive tip [Fig. 4(e)] the spacing between the resonances increases when tip gets close to the center of the QPC, indicating that the area encircled by the current is decreased. The present calculations confirm the interpretation of Ref. 36 that the reduced period of G oscillations for the repulsive tip is a signature of the presence of QHI inside the QPC. Note, that the spacings between B values – already in the absence of the tip are not exactly equal (see Fig. 7 for $U_{\text{tip}} = 0$), which results from the softness of the assumed QHI potential. For $B > 0$ the current circulates counter-clockwise around the QHI [see Fig. 5(b-g)]. The Lorentz force pushes the electron density to the left of the current. For higher magnetic field the shift of the electron density to the center of QHI is stronger, hence

the reduced area of the loop [cf. Fig. 5(b) and (d)] and the increased Aharonov-Bohm period.

The change of the Aharonov-Bohm period with the presence of the tip results from superposition of the two potentials: the one of the defect forming the QPC and the tip potential. We find that in order for this superposition to be effective in the modulation of the B period the potential of the defect needs to be soft. We have performed calculations for a hard-wall QHI potential simulated by

$$V_{\text{QHI}}(x, y) = U_{\text{QHI}} e^{-[(x-x_{\text{QHI}})^2 + (y-y_{\text{QHI}})^2]/r_{\text{QHI}}^8}. \quad (9)$$

For the purpose of the hard-wall simulation we adopted $U_{\text{QHI}} = 10$ meV exceeding by 4 meV the Fermi energy, and $r_{\text{QHI}} = 70$ nm. The results for the scan along the path marked in Fig. 1 by the dashed line are given in Fig.

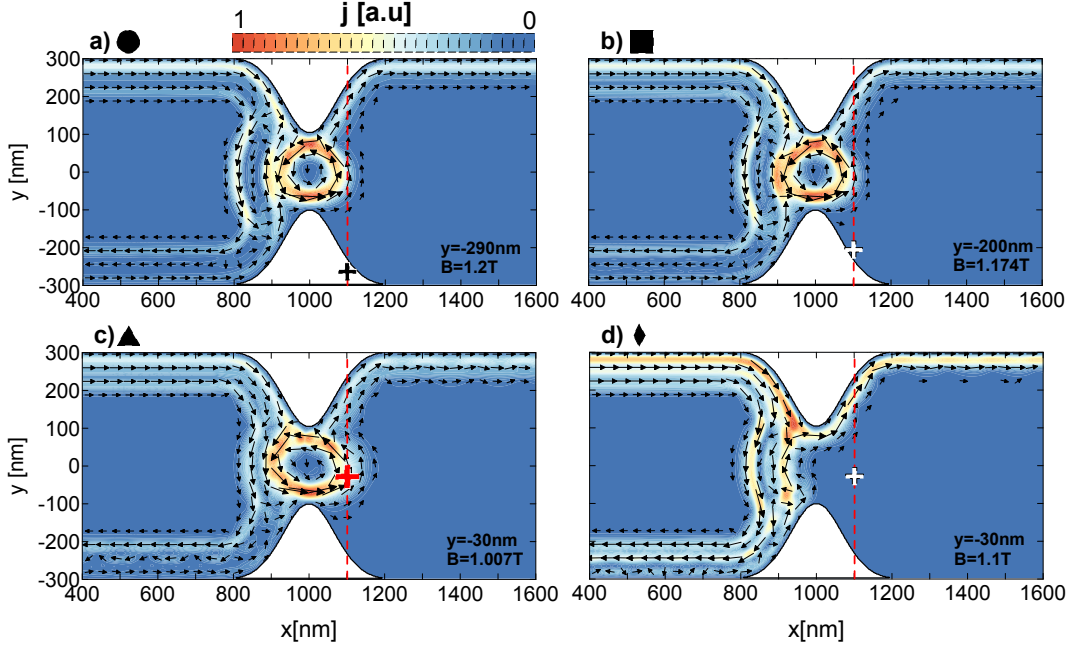


Figure 6: (a-c) Probability density current distribution (color scale shows the absolute value, and the arrows – the orientation of the current) corresponding to points marked by symbols in the conductance scan of Fig 4(d). The position of the tip is marked by cross.

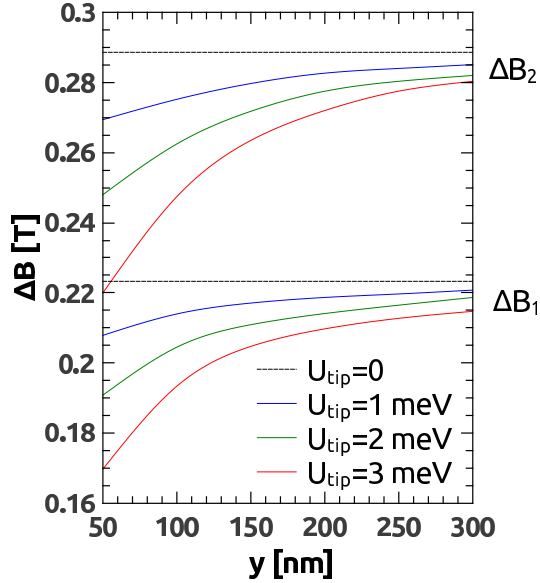


Figure 7: ΔB dependence on the position y of the tip for different values of U_{tip} as extracted from Fig. 4(b-d). For the definition of ΔB_1 and ΔB_2 see Fig. 4(d).

8. In contrast to the results with the soft QHI potential of Fig. 4 we notice that i) in the absence of the tip ($y = 400$ nm) the subsequent G resonances at the B scale are spaced by periods which change with the magnetic field much more slowly than for the soft QHI defect and ii) the presence of the tip shifts the position of the resonances but does not change their spacing significantly as it was

the case for the soft QHI defect.

IV. SUMMARY AND CONCLUSIONS

We have simulated scanning gate microscopy mapping of conductance of both a clean QPC and the one turned into an electron interferometer by a local maximum of the potential landscape in the integer quantum Hall regime. We have solved the quantum scattering problem as given by the Schrödinger equation using a direct finite difference approach with an implementation of the quantum transmitting boundary method. We have described the stepwise reduction of conductance that is due to the tip for clean QPC as well as formation of resonant current loops around the potential defect when introduced to the constriction. We found that the repulsive tip reduces the period of the Aharonov-Bohm-like conductance oscillations for the interferometers. We demonstrated that the periodicity of AB oscillations reacts to the tip only when the potential defect within QPC has a soft character. The presented results for the conductance maps are consistent with the recent experimental results for both clean QPCs and the electron interferometer.

Appendix

This Appendix contains the details of the implementation of the quantum transmitting boundary method for the finite difference approach. After Refs. 43,44 we mul-

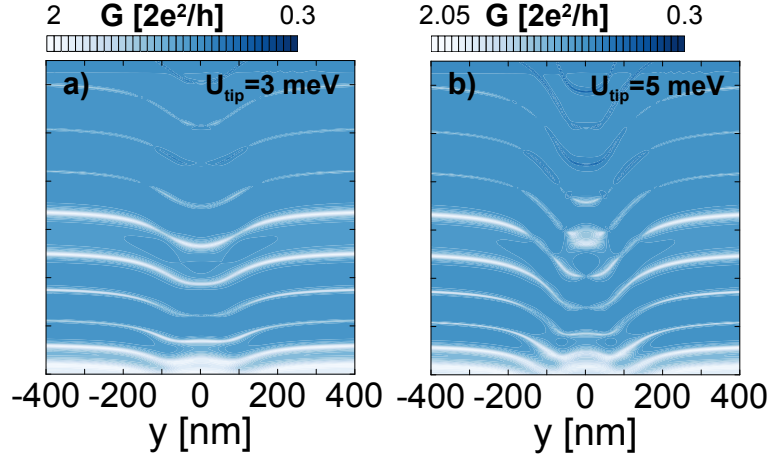


Figure 8: Same as Fig. 4 only for the hard-wall profile of the QHI [Eq. (9)].

tiply both sides of Eq. (5) by a complex conjugate of the m -th outgoing transverse mode χ_{-m} , then we integrate both sides along the channel, putting $x = 0$

$$\langle \chi_{-m}, \Psi \rangle = \sum_{k=1}^M a_k \langle \chi_{-m}, \chi_k \rangle + b_k \langle \chi_{-m}, \chi_{-k} \rangle, \quad (10)$$

where $\langle A, B \rangle = \Delta x \sum_{j=1}^{N_y} A_j^* B_j$ is a standard inner product calculated for the transverse wave function across the channel, here written in finite difference formalism. Equation (10) can be written as system of M -th linear equations for outgoing amplitudes b_k

$$\mathbf{v} = \mathbf{A}\mathbf{a} + \mathbf{S}^{-1}\mathbf{b}, \quad (11)$$

with $v_m = \langle \chi_{-m}, \Psi \rangle$, $A_{mk} = \langle \chi_{-m}, \chi_k \rangle$, $S_{mk}^{-1} = \langle \chi_{-m}, \chi_{-k} \rangle$, $\mathbf{a} = (a_1, a_2, \dots, a_M)^T$, and $\mathbf{b} = (b_1, b_2, \dots, b_M)^T$.

Note, that the different lateral modes χ_k are not orthogonal in presence of the external magnetic field,⁴² and thus \mathbf{S}^{-1} and its inverse matrix are not diagonal. We use Eq. (11) to express vector \mathbf{b} in terms of the incident amplitudes

$$\mathbf{b} = \mathbf{S}\mathbf{v} - \mathbf{S}\mathbf{A}\mathbf{a},$$

with

$$b_k = \sum_{p=1}^M S_{kp} \left\{ \langle \chi_{-p}, \Psi \rangle - \sum_{q=1}^M A_{pq} a_q \right\}. \quad (12)$$

In order to apply the boundary conditions for Eq. (4), we calculate the derivative of Eq. (5) at $x = 0$ ($u = 1$) using the standard central finite difference formula for first order derivative

$$\left. \frac{\partial \Psi}{\partial x} \right|_{u=1} = \frac{\Psi_{2,j} - \Psi_{0,j}}{2\Delta x} = \sum_{k=1}^M \Delta_k a_k \chi_k(j) - \Delta_k b_k \chi_{-k}(j), \quad (13)$$

where

$$\Delta_k = \frac{e^{ik\Delta x} - e^{-ik\Delta x}}{2\Delta x} = -\Delta_{-k}.$$

Now we put the Eq. (12) to the Eq. (13), where we also use the formula for inner product

$$\langle \chi_{-m}, \Psi \rangle|_{u=1} = \Delta x \sum_{i=1}^{N_y} \chi_{-m}^*(j) \Psi_{1,i},$$

we get

$$\begin{aligned} \frac{\Psi_{2,j} - \Psi_{0,j}}{2\Delta x} &= \sum_{k=1}^M \Delta_k \left[a_k \chi_k(j) - \chi_{-k}(j) \sum_{p=1}^M S_{kp} \left\{ \langle \chi_{-p}, \Psi \rangle - \sum_{q=1}^M A_{pq} a_q \right\} \right], \\ &= \sum_{k=1}^M \Delta_k a_k \chi_k(j) + \sum_{k=1}^M \Delta_k \chi_{-k}(j) \sum_{p=1}^M S_{kp} \sum_{q=1}^M A_{pq} a_q \\ &\quad - \Delta x \sum_{i=1}^{N_y} \Psi_{1,i} \cdot \sum_{k,p=1}^M \chi_{-p}^*(i) S_{kp} \chi_{-k}(j) \Delta_k = F_j - \Delta x \sum_{i=1}^{N_y} \alpha_i^j \Psi_{1,i}, \end{aligned}$$

where

$$F_j = \sum_{k=1}^M \Delta_k a_k \chi_k(j) + \sum_{k=1}^M \Delta_k \chi_{-k}(j) \sum_{p,q=1}^M S_{kp} A_{pq} a_q,$$

$$\alpha_i^j = \sum_{k,p=1}^M \chi_{-p}^*(i) S_{kp} \chi_{-k}(j) \Delta_k.$$

From (Eq. 14) we get

$$\Psi_{0,j} = \Psi_{2,j} - 2\Delta x \left(F_j - \Delta x \sum_{i=1}^{N_y} \alpha_i^j \Psi_{1,i} \right),$$

which we put into the Schrödinger equation (4) in order to apply boundary conditions for nodes with $u = 1$

$$\begin{aligned} & \Psi_{1,v} (4t_0 + V_{1,v} - E_F) - 2t_0 \Re \{C_x\} \Psi_{2,v} - \\ & 2t_0 C_x \Delta x^2 \sum_{i=1}^{N_y} \alpha_i^v \Psi_{1,i} - t_0 (\Psi_{1,v-1} + \Psi_{1,v+1}) = -2t_0 C_x \Delta x F_v, \end{aligned}$$

Since $2t_0 \Delta x^2 = 1/m_{\text{eff}}$, we get

$$\begin{aligned} & \Psi_{1,v} \left(4t_0 + V_{1,v} - E_F - \frac{C_x}{m_{\text{eff}}} \alpha_v^v \right) - 2t_0 \Re \{C_x\} \Psi_{2,v} + \\ & \Psi_{1,v+1} \left(-t_0 - \frac{C_x}{m_{\text{eff}}} \alpha_{v+1}^v \right) + \Psi_{1,v-1} \left(-t_0 - \frac{C_x}{m_{\text{eff}}} \alpha_{v-1}^v \right) - \\ & \sum_{i \neq \{v-1, v, v+1\}}^{N_y} \frac{C_x}{m_{\text{eff}}} \alpha_i^v \Psi_{1,i} = -2t_0 \Delta x C_x F_v, \end{aligned}$$

which is the final formula for the boundary condition for the input lead. Using Eq. (6) and choosing the coordinate frame in which $x = 0$ at nodes with $u = N_x$ we get

$$d_k = \sum_p D_{kp} \langle \chi_p, \Psi \rangle, \quad (14)$$

$$D_{kp}^{-1} = \langle \chi_k, \chi_p \rangle.$$

The same as for the input lead one can show that the boundary condition at the output lead $u = N_x$ is given by formula

$$\begin{aligned} & \Psi_{N_x,v} \left(4t_0 + V_{N_x,v} - E_F - \frac{C_x^*}{m_{\text{eff}}} \beta_v^v \right) - 2t_0 \Re \{C_x\} \Psi_{N_x-1,v} + \\ & \Psi_{N_x,v+1} \left(-t_0 - \frac{C_x^*}{m_{\text{eff}}} \beta_{v+1}^v \right) + \Psi_{N_x,v-1} \left(-t_0 - \frac{C_x^*}{m_{\text{eff}}} \beta_{v-1}^v \right) - \\ & \sum_{i \neq \{v-1, v, v+1\}}^{N_y} \frac{C_x^*}{m_{\text{eff}}} \beta_i^v \Psi_{N_x,i} = 0, \end{aligned}$$

with

$$\beta_i^j = \sum_{k,p=1}^M \chi_p^*(i) D_{kp} \chi_k(j) \Delta_k.$$

Equations (4), (14) and (15) define a set of $N_x N_y$ algebraic equations for unknown nodal values of $\Psi_{u,v}$, which

we solve using the LU method for sparse matrices⁴⁷.

- ¹ R.J. Haug, *Semicond. Sci. Technol.* **8**, 131 (1993).
- ² B.I. Halperin, *Phys. Rev. B* **25**, 2185 (1982).
- ³ B.W. Alphenaar, A.A.M. Staring, H. van Houten, M.A.A. Mabeesoone, O.J.A. Buyk, and C.T. Foxon, *Phys. Rev. B* **46**, R7236 (1992).
- ⁴ M. Büttiker, *Phys. Rev. B* **38**, 9375 (1988).
- ⁵ B.J. van Wees, L.P. Kouwenhoven, C.J.P.M. Harmans, J.G. Williamson, C.E. Timmering, M.E.I. Broekaart, C.T. Foxon, and J.J. Harris, *Phys. Rev. Lett.* **62**, 2523 (1989).
- ⁶ B. Rosenow, and B.I. Halperin, *Phys. Rev. Lett.* **98**, 106801 (2007).
- ⁷ B. Hackens, F. Martins, S. Faniel, C.A. Dutu, H. Sellier, S. Huant, M. Pala, L. Desplanque, X. Wallart, and V. Bayot, *Nature Communications*, **1**, 39 (2010).
- ⁸ F. Martins, S. Faniel, B. Rosenow, M.G. Pala, H. Sellier, S. Huant, L. Desplanque, X. Wallart, V. Bayot, B. Hackens, *New J. Phys.* **15**, 013049 (2013).
- ⁹ B.I. Halperin, A. Stern, I. Neder, and B. Rosenow, *Phys. Rev. B* **83**, 155440 (2011).
- ¹⁰ Y. Zhang, D.T. McClure, E.M. Levenson-Falk, C.M. Marcus, L.N. Pfeiffer, and K.W. West, *Phys. Rev. B* **79**, R241304 (2009).
- ¹¹ D.T. McClure, Y. Zhang, B. Rosenow, E.M. Levenson-Falk, C.M. Marcus, L.N. Pfeiffer, and K.W. West, *Phys. Rev. Lett.* **103**, 206806 (2009).
- ¹² S. Ihnatsenka, and I.V. Zozoulenko, *Phys. Rev. B* **77**, 235304 (2008).
- ¹³ F.E. Camino, W. Zhou, and V.J. Goldman, *Phys. Rev. B* **72**, 155313 (2005); **76**, 155305 (2007).
- ¹⁴ F.E. Camino, W. Zhou, and V.J. Goldman, *Phys. Rev. Lett.* **95**, 246802 (2005).
- ¹⁵ V.J. Goldman, J. Liu, and A. Zaslavsky, *Phys. Rev. B* **77**, 115328 (2008).
- ¹⁶ S. Ihnatsenka, I.V. Zozoulenko, and G. Kirczenow, *Phys. Rev. B* **80**, 115303 (2009).
- ¹⁷ S.W. Hwang, J.A. Simmons, D.C. Tsui, and M. Shayegan, *Phys. Rev. B* **44**, 13497 (1991).
- ¹⁸ C.J.B. Ford, P.J. Simson, I. Zailer, D.R. Mace, M. Yosefin, M. Pepper, D.A. Ritchie, J.E.F. Frost, M.P. Grimshaw, and G.A.C. Jones, *Phys. Rev. B* **49**, 17456 (1994).
- ¹⁹ A.S. Sachrajda, Y. Feng, R.P. Taylor, G. Kirczenow, L. Henning, J. Wang, P. Zawadzki, and P.T. Coleridge, *Phys. Rev. B* **50**, 10856 (1994).
- ²⁰ G. Kirczenow, A.S. Sachrajda, Y. Feng, R.P. Taylor, L. Henning, J. Wang, P. Zawadzki, and P.T. Coleridge, *Phys. Rev. Lett.* **72**, 2069 (1994).
- ²¹ V.J. Goldman, J. Liu, and A. Zaslavsky, *Phys. Rev. B* **71**, 153303 (2005).
- ²² M. Kataoka, C.J.B. Ford, G. Faini, D. Mailly, M.Y. Simmons, D.R. Mace, C.T. Liang, and D.A. Ritchie, *Phys. Rev. Lett.* **83**, 160 (1999).
- ²³ R. Crook, C.G. Smith, M.Y. Simmons, and D.A. Ritchie, *Phys. Rev. B* **62**, 5174 (2000).
- ²⁴ M.A. Topinka, B.J. LeRoy, S.E.J. Shaw, E.J. Heller, R.M. Westervelt, K.D. Maranowski, and A.C. Gossard, *Science* **289**, 2323 (2000).
- ²⁵ M.A. Topinka, B.J. LeRoy, R.M. Westervelt, S.E.J. Shaw, R. Fleischmann, E.J. Heller, K.D. Maranowski, A.C. Gossard, *Nature*, **410**, 183 (2001).
- ²⁶ M.P. Jura, M.A. Topinka, L. Urban, A. Yazdani, H. Shtrikman, L.N. Pfeiffer, K.W. West, and D. Goldhaber-Gordon, *Nat. Phys.* **3**, 841 (2007).
- ²⁷ A.A. Kozikov, D. Weinmann, C. Rössler, T. Ihn, K. Ensslin, C. Reichl, and W. Wegscheider, *New J. Phys.* **15**, 083005 (2009).
- ²⁸ H. Sellier, B. Hackens, M.G. Pala, F. Martins, S. Baltazar, X. Wallart, L. Desplanque, V. Bayot, and S. Huant, *Sem. Sci. Tech.* **26**, 064008 (2011); D.K. Ferry, A.M. Burke, R. Akis, R. Brunner, T.E. Day, R. Meisels, F. Kuchar, J.P. Bird, and B.R. Bennett, *Sem. Sci. Tech.* **26**, 043001 (2011).
- ²⁹ K.E. Aidala, R.E. Parott, T. Kramer, E.J. Heller, R.M. Westervelt, M.P. Hanson, and A.C. Gossard, *Nat. Phys.* **3**, 464 (2007).
- ³⁰ N. Paradiso, S. Heun, S. Roddaro, L.N. Pfeiffer, K.W. West, L. Sorba, G. Biasiol, F. Beltram, *Physica E* **42**, 1038 (2010).
- ³¹ J. Rychen, T. Vančura, K. Ensslin, W. Wegscheider, M. Bichler, *Physica E* **13**, 671 (2002).
- ³² S. Kičin, A. Pioda, T. Ihn, K. Ensslin, D.D. Driscoll, and A.C. Gossard, *Physica E* **21**, 708 (2004).
- ³³ N. Aoki, C.R. Cunha, R. Akis, D.K. Ferry, Y. Ochiai, *Phys. Rev. B* **72**, 155327 (2005).
- ³⁴ T. Ihn, J. Rychen, T. Vancura, K. Ensslin, W. Wegscheider, M. Bichler, *Physica E* **13**, 671 (2002).
- ³⁵ A. Pioda, S. Kicin, D. Brunner, T. Ihn, M. Sigrist, K. Ensslin, M. Reinwald, and W. Wegscheider, *Phys. Rev. B* **75**, 045433 (2007).
- ³⁶ F. Martins, S. Faniel, B. Rosenow, H. Sellier, S. Huant, M. G. Pala, L. Desplanque, X. Wallart, V. Bayot, and B. Hackens, *Nature Scientific Reports* **3**, 1416 (2013).
- ³⁷ N. Paradiso, S. Heun, S. Roddaro, L. Sorba, F. Beltram, G. Biasiol, L. N. Pfeiffer, and K. W. West, *Phys. Rev. Lett.* **108**, 246801 (2012).
- ³⁸ B. Szafran, *Phys. Rev. B* **84** 075336 (2011).
- ³⁹ T. Chwiej, and B. Szafran, *Phys. Rev. B* **87**, 085302 (2013).
- ⁴⁰ K. Kolasinski, and B. Szafran, *Phys. Rev. B* **88**, 165306 (2013).
- ⁴¹ M. Governale, and C. Ungarelli, *Phys. Rev. B* **58**, 7816 (1998).
- ⁴² S. Datta, *Electronic Transport in Mesoscopic Systems* (Cambridge University Press, Cambridge, England, 1995).
- ⁴³ D.J. Kirkner, and C.S. Lent, *Journal of Applied Physics* **67**, 6353 (1990).
- ⁴⁴ M. Leng, and C. S. Lent, *Journal of Applied Physics* **76**, 2240 (1994).
- ⁴⁵ J. Huang, C.C. Weng, T. Min, and J. Lijun, *IEEE Trans. Electron Devices* **59**, 468 (2012).
- ⁴⁶ B. Szafran and F.M. Peeters, *Europhys. Lett.* **70**, 810 (2005).
- ⁴⁷ J.W. Demmel, S.C. Eisenstat, J.R. Gilbert, X.S. Li, and J.W.H. Liu, *SIAM. J. Matrix Anal. Appl.* **20**, 720 (1999).